

Direct Magnetic Resonance Imaging of Histological Tissue Samples at 3.0T

Mark D. Meadowcroft,^{1–3} Shutong Zhang,³ Wanzhan Liu,⁴ Bu Sik Park,¹ James R. Connor,⁵ Christopher M. Collins,¹ Michael B. Smith,¹ and Qing X. Yang^{1,5*}

Direct imaging of a histological slice is challenging. The vast difference in dimension between planar size and the thickness of histology slices would require an RF coil to produce a uniform RF magnetic (B_1) field in a 2D plane with minimal thickness. In this work a novel RF coil designed specifically for imaging a histology slice was developed and tested. The experimental data demonstrate that the coil is highly sensitive and capable of producing a uniform B_1 field distribution in a planar region of histological slides, allowing for the acquisition of high-resolution T_2 images and T_2 maps from a 60- μm -thick histological sample. The image intensity and T_2 distributions were directly compared with histological staining of the relative iron concentration of the same slice. This work demonstrates the feasibility of using a microimaging histological coil to image thin slices of pathologically diseased tissue to obtain a precise one-to-one comparison between stained tissue and MR images. *Magn Reson Med* 57:835–841, 2007. © 2007 Wiley-Liss, Inc.

Key words: NMR microscopy/microimaging; RF coil design; coregistration; histology; B_1 field

Magnetic resonance imaging (MRI) has been applied to a variety of in vivo applications because of its ability to provide high and versatile soft-tissue contrast. However, interpretations of the changes in observed image contrast associated with experimental interventions or pathological conditions need to be validated histologically. When comparing MR images with histological results, a tissue sample of a given organ in whole or in part is traditionally imaged first and then cut, stained, and compared with MR images of selected slices (1). This presents a challenge when correlating histological results with MR images because precise coregistration of tissue samples with MR images is notoriously difficult. This method requires that

the histological samples be cut in the same planar orientation as the MR images. Alternatively, previous investigations utilized 3D MR scans to create rotatable 3D MR models of tissue blocks, which allowed for the rotation of the image slice into a specific orientation with a visual inspection in order to compare to traditional 2D or confocal 3D histological images (2,3). This kind of coregistration process is time-consuming and prone to human errors and subjective variability. In addition, the slice thickness of an MR image is generally much larger than the histological tissue slice, resulting in a mismatch between the MRI and histological results. In this case a number of histological slices have to be cut sequentially and assessed as if they were stacked upon each other to match the thickness of one MR slice selection. With this approach, it is difficult to perform a quantitative analysis and comparison of MR images with histology.

Ideally, precise correlation between tissue histology and MRI studies could be obtained using the same tissue sample for both analyses. The implementation of such an approach would require the design and construction of a specific RF coil that could directly image a thin slice of histological sample. In optimization of an RF coil for this purpose, it is particularly important to obtain an adequate signal-to-noise ratio (SNR) because of the small voxel size and the minute volume of tissue being imaged (on the order of $4.5 \times 10^{-3} \text{ cm}^3$) (4,5). To increase the SNR of an image, it is necessary to maximize the filling factor of the coil, which in turn requires an RF coil design that conforms to the geometry of the histological slice. The vast aspect ratio between planar size and the thickness of the histology slice require that the coil design criteria include the production of a uniform B_1 field in a 2D plane with minimal thickness to maximize the filling factor of the coil (6). In this report we present a novel RF coil design that is capable of imaging thin histological tissue sections and thus allows a direct comparison of histological and MR images of the same tissue sample.

MATERIALS AND METHODS

The histological coil was designed and optimized with the aid of computer modeling using XFDTD 6.3 (Remcom, State College, PA, USA). The initial coil design was based on the flat slotted-tube resonator described by Bobroff and McCarthy (7), which consists of two rectangular parallel plates connected by one 664 pF capacitor at each of the four corners. The optimized RF coil design consisted of a 24-mm-wide U-shaped conductor strip wrapped around a dielectric material with a relative permittivity of $\epsilon_r = 5$, simulating two stacked #1 thickness glass coverslips ($24 \times 30 \times 0.150 \text{ mm}$) used to hold histological slices. The open

¹Center for NMR Research, Department of Radiology, Pennsylvania State University College of Medicine, Milton S. Hershey Medical Center, Hershey, Pennsylvania, USA.

²Department of Neural Science and Behavioral Sciences, Pennsylvania State University College of Medicine, Milton S. Hershey Medical Center, Hershey, Pennsylvania, USA.

³Department of Engineering and Applied Science, University of Pennsylvania, Philadelphia, Pennsylvania, USA.

⁴Center for Magnetic Resonance Research, Department of Radiology, School of Medicine, University of Minnesota, Minneapolis, Minnesota, USA.

⁵Department of Neurosurgery, Pennsylvania State University College of Medicine, Milton S. Hershey Medical Center, Hershey, Pennsylvania, USA.

Grant sponsor: Bioengineering Research Partnership/NIH; Grant number: 5R01EB000459-4; Grant sponsor: George M. Leader Foundation.

*Correspondence to: Qing X. Yang, Ph.D., Center for NMR Research, Department of Radiology, M.S. Hershey Medical Center, 500 University Drive, Hershey, PA 17033. E-mail: qyang@psu.edu

Received 17 August 2006; revised 3 January 2007; accepted 15 January 2007.

DOI 10.1002/mrm.21213

Published online in Wiley InterScience (www.interscience.wiley.com).

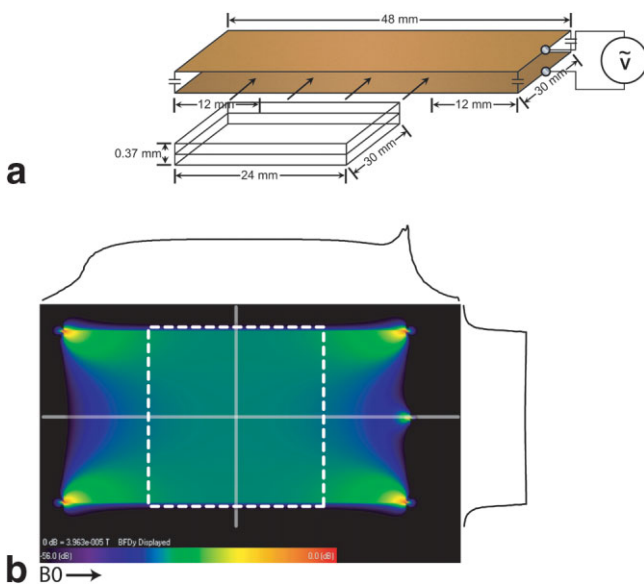


FIG. 1. **a:** Schematic of the flat slotted-tube resonator. Two separate copper strips are connected by a capacitor at each of the four corners. **b:** Calculated transverse B_1 field component perpendicular to B_0 in the center plane of the coil. The imaging region where the glass coverslips are placed is outlined by the white dashed box. The profiles of the B_1 field along the cross hairs through the imaging region are shown above and to the right of the B_1 map. The direction of the B_0 field is noted to aid in the orientation of the coil within the magnet.

end of the U-shaped coil was connected to a voltage driving port. A square slab ($24 \times 24 \times 0.3$ mm) of dielectric material simulating Teflon with a relative permittivity of $\epsilon_r = 2$ was placed between the perfect conductor strips next to the glass coverslips and driving port to provide distributed capacitance for the coil. This design results in a single loop of 24-mm-wide copper strip tightly fitted around the histological slides. The B_1 -field distribution and electromagnetic properties of the flat parallel-plate resonator and the histological coil were calculated and evaluated after the coil models were tuned numerically to 125.44 MHz with a sinusoidal wave from a 50-ohm voltage source placed along the driving port. The total mesh size of both models consisted of 2,162,560 Yee cells with 0.3 mm in each dimension. The schematics of the initial flat slotted-tube resonator and the optimized histological coil design, and their corresponding calculated B_1 -field distributions are shown in Figs. 1 and 2, respectively.

An RF coil was constructed following the optimized histological coil design. The coil was tuned and matched to 125.44 MHz and evaluated on a 3.0T MRI system (Bruker BioSpin GmbH, Ettlingen, Germany). The Q -factor of the coil was measured with a Hewlett-Packard network analyzer. It was approximately 290 when unloaded, and remained unchanged when loaded with a uniform phantom. The homogeneity of the coil was evaluated with two phantoms produced by placing either 12.5 μ l or 43.2 μ l of 0.9% type A agar (Sigma, St. Louis, MO, USA) between two coverslips. Agar results in a nearly uniform distribution of water throughout a sample and is an ideal test for image homogeneity. The 12.5- μ l phantom was nearly cir-

cular and approximated the dimensions of histological brain samples within the imaging region. The 43.2- μ l phantom was used to image the entire 24 mm \times 24 mm coil region, since this amount of agar was calculated to fill the space of two 24 mm \times 30 mm coverslips at a 60- μ m thickness. To evaluate the B_1 -field homogeneity of the coil with an experimental B_1 -field map, we acquired two gradient-echo images from the phantom with flip angles = 90° and 45°, TR = 100 ms, TE = 5.2 ms, NEX = 192, field of view (FOV) = 40 mm \times 40 mm, and matrix size = 128 \times 128, for an imaging time of 41 min each. From these two images the B_1 -field map in the phantom sample was calculated following the method of Stollberger and Wach (8). Subsequently, histological brain-tissue sections taken from a donated Alzheimer's disease (AD) brain specimen were used to evaluate the coil. The tissue samples were fixed with 4% paraformaldehyde, sectioned at 60 μ m using a Leica cryostat, rinsed in phosphate-buffered saline (PBS) to leach out the paraformaldehyde, and then placed between two #1-thickness glass coverslips. To maintain tissue hydration, 25 μ l of PBS were placed onto the tissue. A hydrophobic barrier pen was used at the edge of the coverslips to keep the interior region between the coverslips from desiccating during imaging. All of the images had an FOV of 23 mm \times 23 mm and a matrix size of 128 \times 128, resulting in an in-plane voxel resolution of 179 μ m².

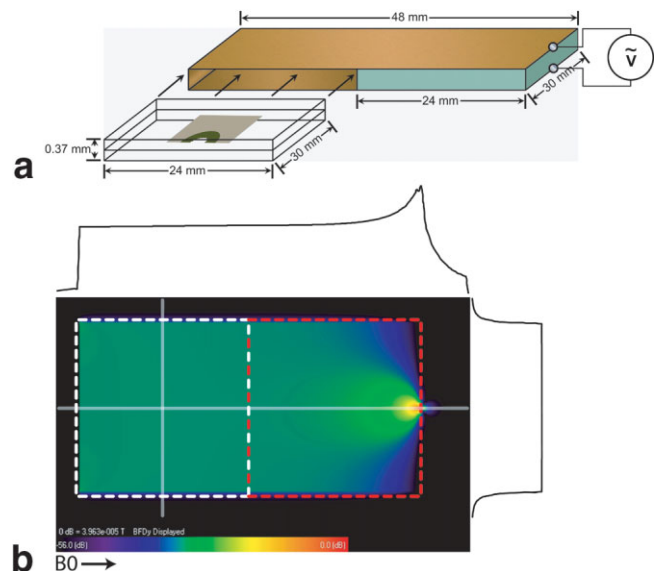
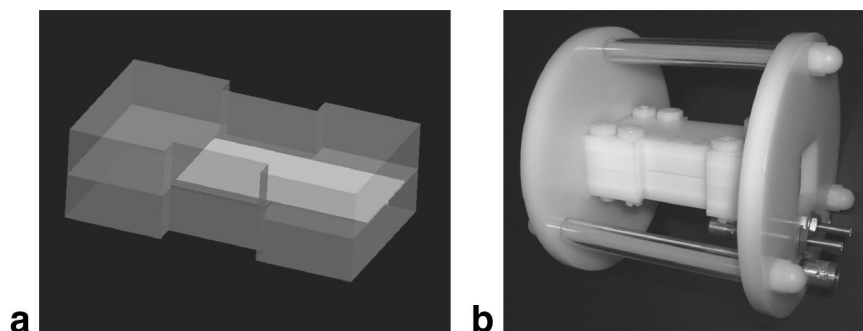


FIG. 2. **a:** Schematic of the optimized histological coil. A continuous strip of copper is wrapped around the glass coverslips and a piece of Teflon (green). Two glass coverslips with the histological sample encased between them are inserted into the opening of the coil for tissue loading. **b:** Calculated transverse B_1 field perpendicular to B_0 in the center plane of the histological coil. The imaging region where the glass coverslips are placed is enclosed in the white dashed line. The profiles along the cross hairs demonstrate the homogeneity of the coil. The red outlined box represents the region where the Teflon is placed. The color scales in Fig. 1b and 2b are set the same to facilitate comparison between the two designs. The profiles in Fig. 1b and 2b indicate that the homogeneity of the B_1 field is improved with the optimized histological coil design. The direction of the B_0 field is noted to aid in the orientation of the coil within the magnetic field.

FIG. 3. **a**: Computer model of the histological coil. The Delrin acetal resin where the coil is positioned is represented by the semitransparent object. **b**: Photograph of the completed coil with the 370- μm opening on the side where the tissue sample and coverslips are inserted along with tuning and matching variable capacitors and BNC connector at the end.



The 60- μm through-plane resolution (defined by the thickness of the sliced tissue) resulted in an overall voxel size of 179 $\mu\text{m} \times 179 \mu\text{m} \times 60 \mu\text{m}$. Fast spin-echo (FSE) T_2 images were obtained using the same geometric parameters with TR = 2500 ms, TE = 12 ms, NEX = 128, and 16 segmented acquisitions for a total image time of 92 min. Multi-SE images were acquired with TR = 1200 ms, TE = 10 ms, bandwidth = 40 kHz, and NEX = 64 with 12 echoes, for a total imaging time of approximately 3 hr. T_2 -weighted images were generated by summation of the amplitude images from all of the echoes to improve the image SNR. T_2 maps were calculated from the multi-SE data with a linear regression method (Chips2005 software; Children's Hospital Image Processing System, Cincinnati, OH, USA) in IDL6.1 (Research Systems, Inc., Boulder, CO, USA). The first echo image was removed for the T_2 calculation to reduce the T_1 effect. After the imaging studies were completed, the brain-tissue samples were stained for iron load with a modified Perl's Prussian blue stain with 1,3-Diaminobenzene back-staining (Sigma, St. Louis, MO, USA).

Figure 1 illustrates the design of the flat slotted-tube resonator and the corresponding calculated B_1 -field map. With such a small coil size, the B_1 field of this design becomes very inhomogeneous because of the connections to the capacitor at each of the corners. Due to the small dimensions of the coil, the current distribution near the feeding points and capacitive elements becomes a determining factor for B_1 -field homogeneity over the entire image plane. This problem was overcome by our optimized coil design depicted in Fig. 2 along with the corresponding calculated B_1 -field map. The two plates were formed with

a continuous copper strip folded above and below the sample. This reduced the field inhomogeneity by eliminating four capacitive element connections. In addition, the plates were extended over a region filled with dielectric material to form a distributed capacitor. The thickness of the 24 \times 24 mm Teflon piece was 0.370 mm, which resulted in a total capacitance of 26.5 pf. As demonstrated in Fig. 2b, with this design the coil produced a nearly perfect homogeneous B_1 distribution over the imaging region outlined by the dashed white box. A comparison of the B_1 -field profiles along the cross hairs in Figs. 1b and 2b indicates that the histological coil's B_1 field has a greater magnitude and is more uniform within the imaging region than the parallel-plate resonator in both dimensions. Construction was completed with Delrin around the copper strip, as shown in both the computer model and the photograph of the coil in Fig. 3. Additional simulations performed with the Delrin enclosure showed that Delrin did not have a noticeable effect on the B_1 field between the copper plates within the imaging region.

To experimentally demonstrate the sensitivity and B_1 -field homogeneity of the optimized histological coil, a T_2 -weighted image and B_1 -field map were obtained from the two uniform agar phantoms shown in Fig. 4a and b, respectively. As indicated by the images and the signal intensity profiles along the two center orthogonal lines, the image intensity and the B_1 field of our coil are uniform over the entire imaging plane. The average SNR of the phantom image in Fig. 4a is approximately 51. Figure 5 shows a T_2 -weighted image obtained with the coil along with a histological image of the same brain slice. The MR image in Fig. 5a yields an average SNR of 65. In the

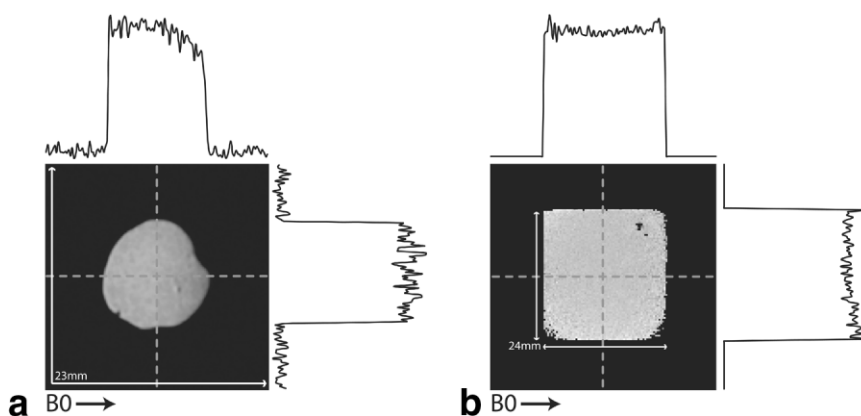


FIG. 4. **a**: T_2 -weighted image obtained with the histological coil of the 12.5- μl phantom approximating the size of a tissue sample. Profiles through the horizontal and vertical center of the phantom are presented on the top and to the side of the image. **b**: B_1 -field map of the 43.2- μl phantom with profiles demonstrating the B_1 -field uniformity of the coil within the imaging region. There are signal dropouts at the bottom two corners due to the drying of the agar sample, and two small artifacts due to air bubbles within the sample.

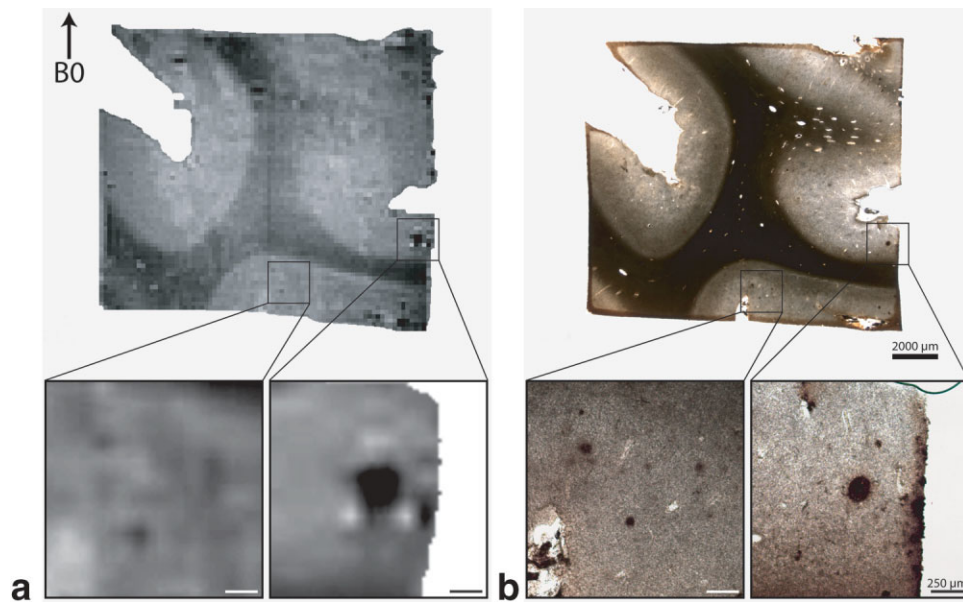


FIG. 5. **a:** T_2 -weighted image of a 60- μm -thick slice of human brain tissue. **b:** Image of the same tissue section stained after MRI with modified Perl's Prussian blue for iron content. Dark regions are indicative of higher iron concentration within the tissue. The correlation of iron content with T_2 contrast is shown in the images (the WM shows up as darker on the T_2 image and high in iron with the histological stain; conversely, GM regions show up as brighter on the T_2 image and lower in stained iron concentration). The 50 \times digital enlargement of the MR image and 50 \times optical bright-field magnification at the bottom demonstrate the close relationship between iron deposition and T_2 content. The regions of highly focal cellular iron concentration in the magnified histological image are clearly seen as darker spots in the MR image. The relative size of the iron deposition affects the magnitude of the hypointensities in the MR image. A typical arrowhead-type imaging artifact is visible around the large hypointensity in the digitally enlarged MR image. Staining artifacts at the edges of the tissue sample due to increased edge surface area are not indicative of higher iron content. Scale bars of 2000 μm for the whole-tissue images and 250 μm for the 50 \times magnified images are included for reference. The direction of the B_0 field is noted to aid in the orientation of the slice within the histological coil.

histological image with a modified Perl's stain shown in Fig. 5b, the regions with higher iron concentration (e.g., those in the white matter (WM)) appear as a darker red-brown. For finer detail, the magnified regions of interest (ROIs) at the bottom of Fig. 5 were digitally postprocessed to 50 \times magnification for the MR images (Fig. 5a) and photographed at 50 \times optical magnification for the bright-field histological image (Fig. 5b). The figure demonstrates that regions with higher focal iron concentration correspond to those having darker intensity in the MR image. High iron concentration is known to cause faster T_2 relax-

ation, which leads to hypointensities in T_2 -weighted images. With our approach, the iron concentration shown in the histological analysis correlates to T_2 contrast in MR images in a straightforward fashion.

With the high B_1 -field homogeneity produced by the histological coil, it is possible to obtain an accurate measurement of T_2 relaxation distribution in a histological tissue sample. Figure 6 shows a representative T_2 parameter map (Fig. 6a) and average relaxation curves (Fig. 6b) from the two ROIs selected within the WM and gray matter (GM) from six tissue samples. The T_2 map exhibits a uni-

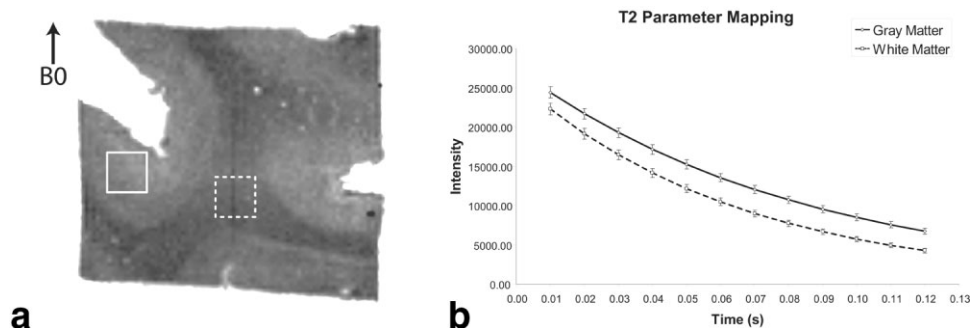


FIG. 6. **a:** T_2 parameter map generated from the same histological slice data shown in Fig. 5a. ROIs were selected in GM (solid box) and WM (dashed box) from six individual maps. **b:** Average T_2 relaxation curves ($N = 6$) with SD bars of each echo image from the ROIs. The average T_2 in the ROI is 85.5 ± 2.4 ms for GM and 66.1 ± 1.5 ms for WM. The direction of the B_0 field is noted to aid in the orientation of the slice within the histological coil.

form distribution within the same tissue type over the slice, indicating an absence of “bias field” interference due to RF field inhomogeneity. Conversely, the T_2 values for different tissue types can be clearly delineated and reliably reproduced over multiple scans. These observations are equivalently evident in the T_2 relaxation curves, which demonstrate clear differences in T_2 decay between ROIs within the two tissue types. Each echo point along the curve has small standard deviations (SDs) in signal intensity between the scans, indicating that the data over the six scans are uniform and reproducible. The T_2 measurements were repeated with the histological coil from six different tissue samples of the same brain and yielded an average T_2 of 85.5 ± 2.4 ms for GM and 66.1 ± 1.5 ms for WM.

DISCUSSION

Numerous NMR microimaging studies have been carried out on various samples with attainable resolutions on the order of several micrometers. Many of these studies used small, traditional birdcage volume coils (9,10), while others employed Helmholtz pair coil designs (11,12). Small, multi-turn solenoid volume and surface coils (13,14) remain the most prevalent design for high-resolution images at ultrahigh field strengths. Our coil, however, was designed specifically to directly image a histological sample between two standard histological #1 glass coverslips. For such an application, the coil design must meet two stringent criteria: 1) given the minute amount of tissue in a histological slide, the coil sensitivity must be maximized. This requires a compact coil design to optimize the filling factor (4) such that coil volume is minimized and the tissue is as close as possible to the conductive coil elements over the entire sample. 2) As a result of the vast difference in aspect ratio between imaging planar size and the thickness of the slice, the coil must produce a homogeneous field distribution within a planar area of $24 \text{ mm} \times 24 \text{ mm}$ in the histological slice. Since these two criteria appear to be mutually exclusive, the difficulty in designing such a coil arises in meeting the two criteria simultaneously. To meet criterion 1, the coil must fit the sample tightly. However, as shown in Fig. 1, the B_1 distribution under such a condition can be dominated by the current around the terminals of the conductive elements because of the size of the coil and the close vicinity of the conductor and sample. These effects are generally insignificant for the overall field homogeneity in the imaging region for human studies because of the relatively large size of the coil and sample. This problem can be alleviated by increasing the planar dimension, as shown in the flat slotted-tube resonator in Fig. 1. With this approach, however, the filling factor of the coil is significantly reduced since the effective coil size is considerably enlarged. In this case the coil sensitivity is reduced as a trade-off for B_1 -field homogeneity. In our coil design, the number of termination points is minimized to a single input pair by using a continuous copper foil and a distributed capacitor. The latter condition is created by efficiently utilizing the space that is necessary for RF field homogeneity between the input port and imaging region. The calculated B_1 field and experimental image profiles in Figs. 2 and 4b are in close

agreement with one another and highlight the nearly perfect homogenous field within the histological coil.

It is evident in Fig. 2 that our design utilizes the far end of the coil region, where the electric field is weakest for imaging, and the region next to the input port, where the electric field is strongest for creating distributed capacitance. A decrease of the electric field in the sample results in a reduction of resistive losses within the sample (6) and an increased Q -factor (15–18), which is desirable for SNR enhancement in microimaging. A coil design that places the tissue sample as close as possible to the coil’s conductor surfaces (within $150 \text{ }\mu\text{m}$, the coverslip thickness) optimizes the filling factor and further enhances SNR (4).

One other major concern in designing a histological coil to optimize RF field homogeneity is the so-called “fringe effect” in a conductor with a high-frequency alternating current. In this case the current distribution concentrates at the edge as the frequency of the alternating field increases. This fringe effect is particularly strong if the conductor is a long flat strip (19). Eddy currents in the conductor that tend to compensate for the magnetic flux changes in space, following Faraday’s law, are responsible for the creation of the fringe effect. As shown in the calculated B_1 -magnitude map in Fig. 2 and demonstrated experimentally in the phantom image in Fig. 4b, the concentration of current along the edges is minimal in our coil design because the copper plates below and above the sample are extremely close, and the currents in them are nearly equal in magnitude and opposite in direction. With such a coil configuration, the magnetic flux in the regions outside the coil above and below the plate is nearly zero, which minimizes the fringe effect in the conductors. This results in a nearly uniform current distribution within the copper plate, and a highly concentrated and uniform magnetic flux density inside the coil. The reduction of eddy currents with our coil design equivalently increases the surface area of the conductor and therefore lowers the resistance to the total current, which increases the coil’s Q -factor (15,20).

This work enables the microimaging and histological staining of the same pathologically diseased tissue sections. Postmortem high-resolution MRI studies of ROIs and comparisons to histology of disease states are important for biomedical research. The accurate comparison between MR and histological images of the same tissue slices has not previously been possible. With our coil design, we acquired MR images from a histological slide of AD brain-tissue sections with high resolution and SNR. The results in Fig. 5 demonstrate that the MR image contrast can associate with a specific histological staining technique. The iron-staining patterns of the tissue samples are in an excellent agreement with the T_2 contrast distribution. Closer histological analysis of the enlarged regions in Fig. 5 suggests that the focal iron deposits may be abnormal accumulations of iron oxide hemosiderin resulting from microbleeds (21,22). Despite the improvements provided by our coil, however, discrepancies between the images acquired with these two different imaging modalities may occur due to sample preparation and various image artifacts, particularly in the MR images. For example, there are two visible dark spots in the left corner of the T_2 images that are not shown in the histological images. These two

dark spots appear to be sandwiched by the two bright pixels above and below, and are most likely magnetic susceptibility artifacts caused by the air bubbles trapped between the two coverslips. Thus, great care must be taken during sample preparation to remove the air pockets between the sample and one of the two glass coverslips. Furthermore, such magnetic susceptibility artifacts could also arise around the focal region of high iron concentration. As shown in the amplified MR image in Fig. 5a, there are three bright spots forming a triangular shape around the dark circular region. While the dark region is clearly seen in the corresponding histological images, indicating a focal high iron concentration, the bright spots are absent in the histological image. The bright spots are typical arrowhead-type imaging artifacts caused by the B_0 -field gradient in the proximity of the focal iron deposit (14,23,24). Hence, when comparing MR and histological images, caution must be exercised to identify the artifacts in MR images and potential morphological alterations of the sample during histological staining.

The ability to create T_2 parametric maps (Fig. 6a) is of importance for comparison of histology with tissue relaxation times. This allows for quantitative studies between ROIs within the same histological slide, and comparisons between normal and diseased tissues. The current results were acquired from at a field strength used in clinical MRI systems, which simplified our analysis for establishment of a more direct relationship between tissue relaxation times and various pathologies. In our experiment, the histological coil assessment of T_2 in formalin-fixed ex vivo human entorhinal cortex ($N = 6$) resulted in 85.5 ± 2.4 ms for GM and 66.1 ± 1.5 ms for WM. Previous in vivo T_2 measurements using the same field strength of 3.0T yielded 109 ms and 79 for GM and WM, respectively (25). The observed reduction in T_2 relaxation from in vivo conditions to formalin-fixed ex vivo measurements follows previously reported results (26,27). Since physical and physiological conditions, such as temperature, diffusion, perfusion, and oxygenation, differ vastly between in vivo tissue and a fixed histological slide, the T_2 values obtained with the histological coil are generally not expected to be identical to the in vivo measurements (26–31). It is not completely understood on a molecular level why the fixation process leads to a drop in T_2 relaxation. In the literature, a number of groups have studied how fixation with formaldehyde affects the T_2 relaxation of tissue samples. It has been observed that the T_2 value of freshly excised brain tissue decays exponentially during the first week of formalin fixation and plateaus following this time period (27). It is known that fixation causes a number of changes in tissue microstructure that affect water motility (28). The main reaction of fixation is believed to be due to the creation of methylene bridges between amino acids in proteins (29). This cross-linking of proteins in turn affects the motility of water in the tissue sample. Following fixation, the alterations in the microstructure of the tissue cause additional barriers to water molecules that make it more difficult for them to cross, resulting in decreased water motility and overall water diffusion (30,31). Imaging of unfixed fresh tissue samples was attempted with the histological coil. However, it was found that thin slices of fresh tissue could not withstand the additional force ex-

erted by the water surface tension between the coverslips. With all of this in mind, caution should be exhibited when comparing quantitative histological coil measurements with in vivo results.

In summary, a novel RF coil specifically designed for direct imaging of a histological slice was developed and tested. The numerical simulation and experimental data demonstrate that the developed coil is highly sensitive and capable of producing a uniform B_1 -field distribution in a planar region of a typical histological slice, allowing for the acquisition of high-resolution T_2 images and T_2 maps from a histological slice. The image intensity and T_2 relaxation map were directly compared with histological staining of relative iron concentration of the same slice. The experimental results demonstrate the feasibility of using our histological coil to image thin slices of tissue and to improve coregistration with histological results. Analysis and comparison between histology of a tissue sample and MRI in a one-to-one fashion is of importance for validating new imaging methods and contrasts, especially in molecular imaging research. Understanding the relationship between a specific pathology and the resulting MRI contrast or quantitative parameters will aid in interpretation of the contrast differentials seen in clinical studies.

REFERENCES

1. Chang C, Jang T. Magnetic resonance microscopy of hamster olfactory bulb: a histological correlation. *Anat Rec* 1995;242:132–135.
2. Rohlfing T, Schaupp F, Haddad D, Brandt R, Haase A, Menzel R, Maurer Jr CR. Unwarping confocal microscopy images of bee brains by nonrigid registration to a magnetic resonance microscopy image. *J Biomed Opt* 2005;10:024018.
3. Breen MS, Lazebnik RS, Wilson DL. Three-dimensional registration of magnetic resonance image data to histological sections with model-based evaluation. *Ann Biomed Eng* 2005;33:1100–1112.
4. Black RD, Early TA, Roemer PB, Mueller OM, Mogro-Campero A, Turner LG, Johnson GA. A high-temperature superconducting receiver for nuclear magnetic resonance microscopy. *Science* 1993;259:793–795.
5. Webb AG. Radiofrequency microcoils in magnetic resonance. *Prog Nucl Magn Reson Spectrosc* 1997;31:1–41.
6. McFarland EW, Mortara A. Three-dimensional NMR microscopy: improving SNR with temperature and microcoils. *Magn Reson Imaging* 1992;10:279–288.
7. Bobroff S, McCarthy MJ. Variations on the slotted-tube resonator: rectangular and elliptical coils. *Magn Reson Imaging* 1999;17:783–789.
8. Stollberger R, Wach P. Imaging of the active B_1 field in vivo. *Magn Reson Med* 1996;35:246–251.
9. Blackband SJ, Bui JD, Buckley DL, Zelles T, Plant HD, Inglis BA, Phillips MI. MR microscopy of perfused brain slices. *Magn Reson Med* 1997;38:1012–1015.
10. Shepherd TM, Scheffler B, King MA, Stanisz GJ, Steindler DA, Blackband SJ. MR microscopy of rat hippocampal slice cultures: a novel model for studying cellular processes and chronic perturbations to tissue microstructure. *Neuroimage* 2006;30:780–786.
11. Banson ML, Cofer GP, Black R, Johnson GA. A probe for specimen magnetic resonance microscopy. *Invest Radiol* 1992;27:157–164.
12. Hall LD, Luck S, Rajanayagam V. Construction of a high-resolution NMR probe for imaging with submillimeter spatial resolution. *J Magn Reson* 1986;66:349–351.
13. Glover PM, Bowtell RW, Brown GD, Mansfield P. A microscope slide probe for high resolution imaging at 11.7 Tesla. *Magn Reson Med* 1994;31:423–428.
14. Bowtell RW, Brown GD, Glover PM, McJury M, Mansfield P. Resolution of cellular structures by NMR microscopy at 11.7 T. *Phil Trans R Soc Lond Biol* 1990;333:457–467.
15. Kneeland JB, Jesmanowicz A, Francisz W, Grist TM, Hyde JS. High-resolution MR imaging using loop-gap resonators. Work in progress. *Radiology* 1986;158:247–250.

16. Grist TM, Hyde JS. Resonators for in vivo 31P NMR at 1.5 T. *J Magn Reson* 1985;61:571–578.
17. Froncisz W, Hyde JS. The loop-gap resonator: a new microwave lumped circuit ESR sample structure. *J Magn Reson* 1982;47:515–521.
18. Hornak JP, Ceckler TL, Bryant RG. Phosphorus-31 NMR spectroscopy using a loop-gap resonator. *J Magn Reson* 1986;68:319–322.
19. Li S, Yang QX, Smith MB. RF coil optimization: evaluation of B1 field homogeneity using field histograms and finite element calculations. *Magn Reson Imaging* 1994;12:1079–1087.
20. Peck TL, Magin RL, Lauterbur PC. Design and analysis of microcoils for NMR microscopy. *J Magn Reson B* 1995;108:114–124.
21. Nakata-Kudo Y, Mizuno T, Yamada K, Shiga K, Yoshikawa K, Mori S, Nishimura T, Nakajima K, Nakagawa M. Microbleeds in Alzheimer disease are more related to cerebral amyloid angiopathy than cerebrovascular disease. *Dement Geriatr Cogn Disord* 2006;22:8–14.
22. Quintana C, Bellefqih S, Laval JY, Guerquin-Kern JL, Wu TD, Avila J, Ferrer I, Arranz R, Patino C. Study of the localization of iron, ferritin, and hemosiderin in Alzheimer's disease hippocampus by analytical microscopy at the subcellular level. *J Struct Biol* 2006;153:42–54.
23. Butts K, Pauly JM, Daniel BL, Kee S, Norbash AM. Management of biopsy needle artifacts: techniques for RF-refocused MRI. *J Magn Reson Imaging* 1999;9:586–595.
24. Glowinski A, Adam G, Buckner A, van Vaals J, Gunther RW. A perspective on needle artifacts in MRI: an electromagnetic model for experimentally separating susceptibility effects. *IEEE Trans Med Imaging* 2000;19:1248–1252.
25. Wansapura JP, Holland SK, Dunn RS, Ball Jr WS. NMR relaxation times in the human brain at 3.0 Tesla. *J Magn Reson Imaging* 1999;9:531–538.
26. Blamire AM, Rowe JG, Styles P, McDonald B. Optimising imaging parameters for post mortem MR imaging of the human brain. *Acta Radiol* 1999;40:593–597.
27. Yong-Hing CJ, Obenaus A, Stryker R, Tong K, Sarty GE. Magnetic resonance imaging and mathematical modeling of progressive formalin fixation of the human brain. *Magn Reson Med* 2005;54:324–332.
28. Pfefferbaum A, Sullivan EV, Adalsteinsson E, Garrick T, Harper C. Postmortem MR imaging of formalin-fixed human brain. *Neuroimage* 2004;21:1585–1595.
29. Helander KG. Kinetic studies of formaldehyde binding in tissue. *Biotechnol Histochem* 1994;69:177–179.
30. Sun SW, Neil JJ, Liang HF, He YY, Schmidt RE, Hsu CY, Song SK. Formalin fixation alters water diffusion coefficient magnitude but not anisotropy in infarcted brain. *Magn Reson Med* 2005;53:1447–1451.
31. Sun SW, Neil JJ, Song SK. Relative indices of water diffusion anisotropy are equivalent in live and formalin-fixed mouse brains. *Magn Reson Med* 2003;50:743–748.